

# Analysis of the Navigation of Magnetic Microrobots through Cerebral Bifurcations for Targeted Drug Delivery

Pedro G. Alves, Maria Pinto, Rosa Moreira, Derick Sivakumaran, Fabian Landers, Maria Guix, Bradley J. Nelson, Andreas D. Flouris, Salvador Pané, Josep Puigmartí-Luis,\* and Tiago S. Mayor\*

Local administration of thrombolytics in ischemic stroke could accelerate clot lysis and the ensuing reperfusion while minimizing the side effects of systemic administration. Medical microrobots could be injected into the bloodstream and magnetically navigated to the clot for administering the drugs directly to the target. The magnetic manipulation that is required to navigate medical microrobots depends on various parameters such as the microrobots size, the blood velocity, and the imposed magnetic field gradients. Numerical simulation was used to study the motion of magnetically controlled microrobots flowing through representative cerebral bifurcations, for predicting the magnetic gradients required to navigate the microrobots from the injection point until the target location. Upon thorough validation of the model against several independent analytical and experimental results, the model was used to generate maps and predictive equations providing quantitative information on the required magnetic gradients, for different scenarios. The developed maps and predictive equations are crucial to inform the design, operation, and optimization of magnetic navigation systems for healthcare applications.

## 1. Introduction


Stroke is characterized by an inadequate blood supply to cerebral tissue, which can lead to long-term disability and death. According to the 2019 Global Burden of Disease study, stroke is the second-leading cause of death worldwide and its incidence has increased by 70% between 1990 and 2019. Of all the worldwide new stroke occurrences in 2019, two-thirds (7.6 million cases) were of the ischemic type.<sup>[1]</sup> Ischemic strokes are characterized by a vascular occlusion that blocks blood flow to downstream arteries, leading to tissue necrosis and serious long-term complications including death.<sup>[2]</sup> The established treatment for ischemic stroke is the systemic administration of thrombolytic agents to dissolve the clot obstructing the artery.<sup>[3,4]</sup> However, only up to 20% of cases respond to treatment as the clots can be too big to

dissolve in a timely manner, due to the systemic administration instead of a localized approach.<sup>[5]</sup> Dosage increase is not possible due to the toxicity and side effects of this type of drug, including

P. G. Alves, T. S. Mayor  
Transport Phenomena Research Centre (CEFT)  
Engineering Faculty  
Porto University  
Rua Dr. Roberto Frias, Porto 4200-465, Porto, Portugal  
E-mail: tiago.sottomayor@fe.up.pt

P. G. Alves, T. S. Mayor  
Associate Laboratory in Chemical Engineering (ALICE)  
Engineering Faculty  
Porto University  
Rua Dr. Roberto Frias, Porto 4200-465, Porto, Portugal

M. Pinto, R. Moreira  
Experian  
Porto 4200-205, Portugal

 The ORCID identification number(s) for the author(s) of this article can be found under <https://doi.org/10.1002/aisy.202400993>.

© 2025 The Author(s). Advanced Intelligent Systems published by Wiley-VCH GmbH. This is an open access article under the terms of the Creative Commons Attribution License, which permits use, distribution and reproduction in any medium, provided the original work is properly cited.

DOI: 10.1002/aisy.202400993

D. Sivakumaran  
Magnebotix  
Rütistrasse 14, Zurich 8952, Schlieren, Switzerland

F. Landers, B. J. Nelson, S. Pané  
Multi-Scale Robotics Lab  
ETH Zürich  
Tannenstrasse 3, Zürich 8006, Switzerland

M. Guix, J. Puigmartí-Luis  
Depart. de Ciència dels Materials i Química Física and Institut de Química Teòrica i Computacional  
University of Barcelona  
Martí i Franquès 1-11, Barcelona 08028, Barcelona, Spain  
E-mail: josep.puigmarti@ub.edu

A. D. Flouris  
FAME Laboratory  
Department of Exercise Science  
University of Thessaly  
Karies, Trikala 42100, Thessaly, Greece

J. Puigmartí-Luis  
Institutió Catalana de Recerca i Estudis Avançats (ICREA)  
Passeig Lluís Companys 23, Barcelona 08010, Barcelona, Spain

blood thinning effects that can lead to bleeding.<sup>[2,6]</sup> Mechanical removal of the clots (or thrombectomy) is an additional approach where a catheter is used to reach into the cerebral arteries to extract the clot and improve recanalization.<sup>[5,7]</sup> Yet, that can be challenging in narrow and tortuous arteries, making it difficult to navigate the catheter to deep locations. Hence, a new approach to reach deep neurovascular regions and locally administer thrombolytic agents is necessary to accelerate clot lysis and reduce potential systemic side effects.

Medical microrobots have been proposed as the perfect candidate for such a task, as they could be injected into the patient's bloodstream, navigated to the desired location, and made to locally deliver a specific drug.<sup>[8,9]</sup> In the last decade, several concepts for the application of microrobots in healthcare have been proposed, such as targeted drug delivery, microbiopsy, ablation, remote sensing, and scaffolding, to name a few.<sup>[10–12]</sup> Yet, some challenges remain. For instance, with the scaling down of microrobots comes a change in the forces acting on them.<sup>[13,14]</sup> Viscous forces and surface effects become more important than volumetric effects such as inertia and weight, which pose constraints on the generation and storage of power for propulsion.<sup>[11,12,14]</sup> Conventional technologies used with larger robots are yet to be scaled down to microsizes,<sup>[11]</sup> propelling researchers to look for novel methods beyond those used in conventional robotics. Magnetic manipulation has gained attention in this context, as it allows for precise steering of magnetic objects to specific locations, can wirelessly transmit power to objects, is externally controlled and biocompatible.<sup>[15]</sup> Several experimental studies using magnetic manipulation systems have been reported, considering different object geometries (e.g., sphere, rod, and helix),<sup>[16–19]</sup> locomotion strategies (i.e., propulsion, rolling, and tumbling),<sup>[17,19]</sup> and magnetic stimuli (i.e., field gradients, rotating fields, and oscillating fields).<sup>[20–22]</sup> Thus, magnetically manipulated microrobots could potentially be navigated through the cerebral arteries using external magnetic field gradients, to deliver therapeutic agents directly to the affected regions (e.g., a clot).

The ability to manipulate microrobots injected in the bloodstream depends on different parameters, such as the microrobots size, the blood flow velocity, and the magnetic field gradients imposed. Most works in the literature include the use of magnets placed near the vessels to capture magnetic microrobots. Kenjereš and colleagues investigated the deposition of microrobots (0.25–4  $\mu\text{m}$ ) in a brain vascular system and concluded that the use of a magnet in the vicinity of the arteries significantly increased the microrobots capture in the targeted regions.<sup>[23]</sup> Cherry and colleagues studied the effect of microrobot size, blood velocity, and magnetic field gradients on the trapping of microrobots (15–50  $\mu\text{m}$ ) in a tube exposed to magnetic field gradients. They observed more trapping with larger microrobot sizes, lower flow velocities, and higher magnetic field gradients.<sup>[24]</sup> Bose and Banerjee simulated the 2D trajectory and capture of microrobots (0.25–4  $\mu\text{m}$ ) in a stenosed artery bifurcation to assess the influence of microrobot size, Reynolds number of the flow, and magnetic field gradients on the capture efficiency.<sup>[25]</sup> They observed that higher microrobot sizes, lower Reynolds number, and higher magnetic field gradients led to higher capture efficiency. Larimi and co-workers studied the trajectory of nanomicrorobots (5–500 nm) in a bifurcation with a magnet close to one of its walls.<sup>[26]</sup> They found that the use of magnets helped to deliver microrobots to

the target, though delivery decreased with increasing flow Reynolds number. Finally, Pourmehran and colleagues studied the delivery of magnetic microrobots through the human tracheobronchial airways and found that delivery to the target was higher with larger microrobot sizes and lower inhalation flow rates.<sup>[27]</sup>

Despite these contributions providing qualitative insight into the influence of various parameters over the magnetic manipulation of microrobots, they are still insufficient to enable the prediction of the magnetic field gradients needed to navigate microrobots along specific paths. Importantly, they focus on the manipulation of very small microrobots (<50  $\mu\text{m}$ ) and provide no quantitative information on how the magnetic gradients should be changed to navigate larger microrobots (50 <  $\varnothing$  < 1000  $\mu\text{m}$ ), whose higher drug-loading capacity would make them more relevant for drug-delivery applications.<sup>[28–30]</sup> Larger microrobots require lower magnetic gradients,<sup>[31]</sup> which can be induced by magnets placed farther apart. This allows for the widening of the workspaces with controlled magnetic gradients, something key for enabling the manipulation of microrobots in workspaces compatible with the human neurovascular network. Yet, the magnetic gradients needed to manipulate large microrobots in such workspaces cannot be easily inferred from the results of the above contributions.

Here we study the motion of microrobots in the blood flowing through representative cerebral bifurcations, to investigate how magnetic gradients can be used to navigate the microrobots from the injection point to a target location. First, we use computational fluid dynamics to numerically simulate the blood flow and predict its effect over the microrobots trajectory. Then, we examine the effect of microrobot diameter, artery geometry, blood velocity, injection point, and target locations, on the magnetic gradients required to navigate the microrobots along the bifurcations. We use these data to develop maps and a predictive equation providing quantitative information on the required magnetic gradients, for each scenario. The developed maps and predictive equations offer easy-to-use information to guide the design, operation, and optimization of automated magnetic navigation systems for healthcare applications.

## 2. Experimental Section

### 2.1. Problem Formulation

The motion of microrobots along bifurcations mimicking cerebral vascular structures was numerically studied to investigate how magnetic gradients can be leveraged to navigate the microrobots to one of the bifurcation branches. A microrobot injected into the bloodstream is affected by various forces (e.g., drag, buoyancy, and gravitational), the net of which will determine its motion through the vascular structures. To define the specific path to be followed by the microrobots when flowing through a bifurcation, we considered intermediate targets, positioned upstream and downstream the point of flow splitting, as well as at the desired outlet of the bifurcation. The magnetic gradients required to navigate the microrobots along the defined paths depend on the microrobot size, artery geometry, blood velocity, position of the intermediate targets, and microrobot

initial position. For this reason, the values of these parameters were varied in a systematic way to study their influence over the required magnetic gradients.

To quantify the success in navigating microrobots along bifurcations, we calculated the navigation success as the ratio between the number of microrobots reaching the target branch, and the total number of microrobots entering the bifurcation. Navigation success thus varied between 0% (no microrobots reaching the target) and 100% (all microrobots reaching the target).

## 2.2. Modeling Assumptions and Boundary Conditions

### 2.2.1. Artery Bifurcations

The bifurcations were modeled in 3D based on the geometries of the anterior, middle, and posterior cerebral arteries, where most of the clots are observed in ischemic stroke.<sup>[32–35]</sup> The diameter and length of the main artery of the bifurcations ( $D_1$  and  $L$  in Figure S1, Supporting Information) were defined based on the values reported in the literature (Table 1),<sup>[36–40]</sup> to capture the main features of the blood flow in the mentioned arteries. The vessels were considered straight and smooth (Figure S1, Supporting Information) to reduce the computational cost of the simulations. The diameter of the branching arteries ( $D_{2-3}$ , Figure S1, Supporting Information) was computed using Murray's law,<sup>[41]</sup> which is based on the principle that the vascular system evolved to minimize the work associated with the blood flow. From Murray's law, the diameter of the main artery can be related to that of the branch arteries as  $D_1^3 = D_2^3 + D_3^3$  (Figure S1, Supporting Information), and thus  $D_{2-3}$  can be computed as  $D_1 \cdot 2^{-1/3}$  when  $D_2 = D_3$ .

### 2.2.2. Blood Flow

Blood was modeled as an incompressible non-Newtonian fluid with shear-thinning behavior<sup>[42]</sup> and a density of  $1060 \text{ kg m}^{-3}$ .<sup>[43]</sup> The apparent viscosity of the blood ( $\eta$ ) was described by the Carreau model,<sup>[44]</sup> given its good agreement with experimental data<sup>[45]</sup> for both low and high shear rates.

$$\eta = \eta_\infty + (\eta_0 - \eta_\infty)[1 + (\lambda\dot{\gamma})^2]^{\frac{n-1}{2}} \quad (1)$$

where  $\dot{\gamma}$  is the shear rate,  $\eta_0 = 0.056 \text{ Pa}\cdot\text{s}$ , and  $\eta_\infty = 0.00345 \text{ Pa}\cdot\text{s}$  are the limits of the apparent viscosity for low and high shear rates, respectively, and  $\lambda = 3.313 \text{ s}$  and  $n = 0.3568$  are fitting parameters.<sup>[46]</sup>

The blood flow was assumed to be laminar, given the associated low Reynolds number ( $50 < \text{Re} < 250$ ), and nonpulsatile, given that steady flow conditions can be used to accurately predict

**Table 1.** Diameters and lengths of the bifurcations considered in this study.

	$D_1$ [mm] <sup>[39,40]</sup>	$D_2 = D_3$ [mm]	$L$ [mm] <sup>[36–38,40]</sup>
anterior cerebral artery (ACA)	2.00	1.59	20
middle cerebral artery (MCA)	2.40	1.90	30
posterior cerebral artery (PCA)	1.80	1.27	10

the blood flow distribution<sup>[47–49]</sup> and many hemodynamic parameters (i.e., flow profile, vorticity, and helicity; more details in Supporting Information).<sup>[50–54]</sup> The blood velocity differs substantially depending on the vessels it flows through.<sup>[42]</sup> Maximum blood velocities of  $0.25$ – $0.45$ ,  $0.35$ – $0.55$ , and  $0.45$ – $0.65 \text{ m s}^{-1}$  were reported for the posterior, anterior, and middle cerebral arteries, respectively, based on measurements on healthy individuals.<sup>[55–58]</sup> For this reason, to investigate a wide range of blood velocities, in this work, we considered five different values of maximum blood velocities between  $0.25$  and  $0.65 \text{ m s}^{-1}$ , in steps of  $0.10 \text{ m s}^{-1}$ , for each of the three arteries considered. The velocity profile of the blood entering the bifurcations was assumed to be fully developed, with the flow development assumed to occur in the vascular structures upstream of the bifurcation inlet. Based on this, the velocity profile at the bifurcation inlet was calculated using<sup>[44]</sup>

$$u_f(r) = u_{f,\max} \left[ 1 - \left( \frac{r}{R} \right)^{\frac{n+1}{n}} \right] \quad (2)$$

where  $r$  is the radial position,  $R$  is the artery radius, and  $n$  is a parameter describing the degree of non-Newtonian behavior. The value of  $n$  was empirically determined to ensure that the velocity profile introduced at the bifurcation inlet (i.e., predicted by Equation (2)) remains unchanged as the blood flows along the main artery of the bifurcation (in line with the assumption of fully developed flow). This was found to occur for  $n = 0.89$ , as expected for shear-thinning fluids, for which  $n < 1$ . No-slip condition was assumed at the walls of the arteries, and zero-gauge pressure was assumed at the outlets of the bifurcation.

### 2.2.3. Microrobots

The microrobots were modeled as discrete sphere whose motion was predicted using a Lagrangian approach, where each microrobot was represented as a point that was tracked in space and time, to plot its trajectory.<sup>[59]</sup> In line with other works in the literature,<sup>[23,26,27,60,61]</sup> a one-way approach was considered to model the interactions between the blood flow and the microrobots, according to which the blood flow was assumed to affect the motion of the microrobots (e.g., through drag force), while their volume was assumed not to affect the flow.<sup>[59]</sup> We chose a one-way approach instead of a two-way approach (in which the flow would affect the motion of the microrobots and their volume would affect the flow), given its much lower computational cost, which was crucial to enable the simulation of thousands of different scenarios in a timely manner.

The microrobots were assumed to consist of magnetic material only (i.e., iron oxide), with a magnetization of  $5 \times 10^5 \text{ A m}^{-1}$  equal to its saturation magnetization ( $M_s$ ),<sup>[24,62]</sup> and a density of  $5200 \text{ kg m}^{-3}$ .<sup>[63]</sup> We chose a magnetic volume equal to the microrobot volume ( $V_M = V_p$ ) and a magnetization equal to the saturation value so that the predicted magnetic gradients corresponded to the minimum gradients that produced a given magnetic force ( $\vec{F}_{\text{Magnetic}}$ )

$$\vec{F}_{\text{Magnetic}} = V_p \cdot M_s \cdot \nabla \vec{B} \Leftrightarrow \nabla \vec{B} = \frac{\vec{F}_{\text{Magnetic}}}{V_p \cdot M_s} \quad (3)$$

where  $V_p$  is the microrobot volume and  $\nabla \vec{B}$  is the magnetic field gradient.<sup>[64]</sup>

The microrobots were considered to have diameters ( $d_p$ ) of 50, 100, 250, 500, and 1000  $\mu\text{m}$ , to investigate a wide range of possible sizes for which the required magnetic gradients are necessarily different. Furthermore, we considered microrobots sizes much larger than those considered in the literature related to magnetic manipulation (where microrobot sizes are typically much smaller than 50  $\mu\text{m}$ ),<sup>[23–27]</sup> given their higher drug-loading capacity, which is relevant for drug-delivery applications.<sup>[28–30]</sup>

The microrobots were assumed to enter the bifurcation at five positions along the diameter of the main artery (Figure S2, Supporting Information, left), namely, at its center (position 3), at each of the artery walls (positions 1 and 5), and halfway between the two (positions 2 and 4). This is important to study the effect of the microrobots initial position on the magnetic gradients needed to navigate them along the bifurcations. The microrobots were assumed to be transported by the blood flow, thus entering the main artery with the blood velocity (Equation (2)) prevailing in the mentioned radial positions (Figure S2, Supporting Information, left).

#### 2.2.4. Intermediate Targets

As the blood flowing along the main artery of a bifurcation splits into each of its daughter branches (Figure 1), a portion of the bloodstream flows through the desired branch, and the rest flows through the opposite branch. For a microrobot to be navigated through the desired branch, it must be on the portion of the bloodstream that is on the same side as the desired branch (left green region, Figure 1), by the time the flow splits. Somewhat upstream of this position, the trajectory of the microrobot must start to be corrected to avoid major collisions with the branch walls (e.g., around the apex of the bifurcation) that could delay its progression. To meet these two requirements, we considered the existence of two intermediate targets, upstream and downstream of the flow splitting. The target upstream of the flow splitting serves to guide the microrobot to the desired portion of the artery (left green region, Figure 1), whereas the target downstream of the flow splitting serves to guide the microrobot

through the desired branch without major collisions with its walls.

To study how the position of the intermediate targets affects the magnetic gradients needed for navigating the microrobots along the bifurcation, we considered four different positions upstream and downstream the flow splitting, defined in relation to the microrobot diameter (i.e.,  $-4D$ ,  $-3D$ ,  $-2D$ , and  $-1D$ , for the upstream positions, and  $+1D$ ,  $+2D$ ,  $+3D$ , and  $+4D$ , for the downstream positions, Figure 1), in a total of 16 possible combinations of target positions. Radially, the intermediate targets were positioned halfway between the center of the arteries and the position at which the microrobots would touch the wall (Figure 1). This is important to guide the microrobots to regions with velocity lower than that at the center (Equation (2))—key for reducing the magnetic gradients needed for navigation—while minimizing the risk of collisions with the walls. The position of the intermediate targets defined three regions of interest (Figure 1, right) for the analysis of the required magnetic gradient, namely, the G1 region (from the inlet to the upstream target), the G2 region (between the upstream and the downstream targets), and the G3 region (from the downstream target to the outlet).

#### 2.2.5. Microrobot-Fluid and Microrobot-Wall Interactions

In a classic one-way approach, the objects transported by the flow are treated as points representing the center of the object, which can occupy any position in the domain, even impossible positions where part of the object volume falls outside the domain boundaries (e.g., artery walls, Figure S2a, Supporting Information). To avoid this problem, in this work, we improved the calculation of the microrobot trajectories by preventing the microrobot centers from being less than one radius away from the artery walls. This constraint implies that the microrobot can touch but not cross the artery walls (Figure S2b, Supporting Information). This is crucial to improve the accuracy of the calculated trajectories compared to the classic one-way approach and is particularly important when collisions with the walls may occur.

When computing the microrobot trajectory with this constraint, a collision occurs when the microrobot center is one radius away from the wall, at which point the trajectory changes due to the impact. Collisions of objects with walls, and their effect over

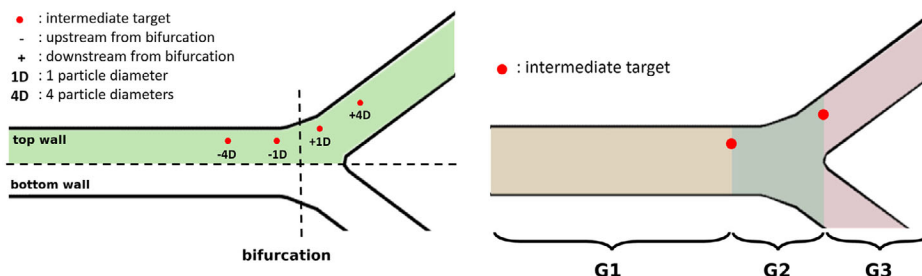


**Figure 1.** Illustration of the positions of the intermediate targets considered to guide the microrobots along the bifurcation (left), highlighting the side of the branch to which the microrobots must be navigated to (green area on the left), and the segmentation of the bifurcation into three main regions defined by the position of the intermediate targets (right). Targets are positioned 1–4 microrobot diameters away from the position of flow splitting (bifurcation), upstream, or downstream of this position, to form a pair. In this illustration, four possible intermediate target pairings are shown:  $-4D+1D$ ,  $-4D+4D$ ,  $-1D+1D$ , and  $-1D+4D$  (left). The flow splitting is assumed to coincide with the end of the main artery of the bifurcation. The positions of the intermediate targets define the limits of each of the three segmentations of the bifurcation, which are useful to determine the magnetic gradients G1, G2, and G3 required in each region (right).



the objects' velocity can be treated via the coefficient of restitution (COR), which describes the degree of elasticity of the collision. In that context, a fully elastic collision (where COR = 1) implies that the object retains all its momentum upon impact, whereas a fully inelastic collision (where COR = 0) implies the object loses all its momentum, remaining attached to the wall after impact. A survey of various numerical works involving collisions of particles with vessels walls<sup>[26,65–67]</sup> indicates that very different values of coefficients of restitution are used (0.25–1.0), without being clear which value is better for describing the situation under study in this work (e.g., the coefficient of restitution strongly depends on the mechanical properties of the objects colliding, which advises caution when trying to compare works with different underlying assumptions). For this reason, in this work we chose a conservative value for the coefficient of restitution, that is, COR = 1, to minimize the footprint of the underlying assumption in the predicted trajectories, because any coefficient of restitution below unity would lead to loss of momentum and larger accumulation of microrobots near the walls, both of which would ultimately delay the progression of the microrobots along the vessels and increase the associated calculation time.

### 2.3. Numerical Methods

The blood flow in the bifurcation models was simulated using a computational fluid dynamics approach based on the finite-volume method.<sup>[68,69]</sup> Blood velocity and pressure were calculated by coupling the continuity equation and the Navier–Stokes equation for an incompressible non-Newtonian fluid, given respectively by

$$\nabla \vec{u}_f = 0 \quad (4)$$

$$\rho_f \frac{\partial \vec{u}_f}{\partial t} = -\nabla p + \eta \nabla^2 \vec{u}_f + \rho_f \vec{g} \quad (5)$$

where  $\vec{u}_f$  is the flow velocity,  $\rho_f$  is the fluid density,  $p$  is pressure,  $\nabla$  and  $\nabla^2$  are the divergence and Laplacian operators, and  $\vec{g}$  is the gravitational acceleration. A steady-state, double-precision, pressure-based solver was used considering second-order discretization and a velocity-pressure coupling. Flow simulations were performed using an unstructured mesh with around  $3.3 \times 10^6$  cells (maximum element size of 0.050 mm), which produced mesh-independent results with low computational cost (Figure S3, Supporting Information). A convergence criterion of  $10^{-6}$  was considered for the continuity, velocity, and viscosity, with stricter criteria producing similar results. An illustration of the unstructured mesh used is shown in Figure S3, Supporting Information.

The microrobot 3D velocity and position were obtained by integration of the force balance between the microrobot inertia and the forces that acted on it over discrete time steps (Equation (6)). The total force acting on a microrobot placed in a flowing fluid can have multiple contributions such as drag, gravity, buoyancy, virtual mass, pressure gradient, Saffmann's

lift, and Brownian motion. The virtual mass and pressure gradient forces are only relevant if  $\rho_f/\rho_p$  is close to the unity<sup>[26]</sup> (in this work  $\rho_f/\rho_p \approx 0.2$ ), and Saffmann's lift and Brownian forces are only relevant for submicrometer microrobots (in this work  $d_p > 50 \mu\text{m}$ ).<sup>[59]</sup> Thus, only the drag, gravity, and buoyancy forces, as well as the external magnetic force, were considered in this work to compute the total (net) force  $\vec{F}_T$  using the force balance equation.<sup>[70]</sup>

$$m_p \frac{d\vec{u}_p}{dt} = m_p \underbrace{\frac{\vec{u}_f - \vec{u}_p}{\tau_p}}_{\vec{F}_{\text{Drag}}} + m_p \underbrace{\frac{\vec{g}(\rho_p - \rho_f)}{\rho_p}}_{\vec{F}_{\text{Gravity}} - \vec{F}_{\text{Buoyancy}}} + \underbrace{V_p \cdot \nabla \vec{B} \cdot M_s}_{\vec{F}_{\text{Magnetic}}} \quad (6)$$

where  $m_p$  is the microrobot mass,  $\vec{u}_p$  is the microrobot velocity,  $t$  is time,  $\tau_p$  is the microrobot relaxation time,  $\rho_p$  is the microrobot density,  $V_p$  is the microrobot volume,  $\nabla \vec{B}$  is the magnetic gradient, and  $M_s$  is the saturation magnetization. Equation (6) is used to calculate the net force acting on the microrobot, when navigated in the bloodstream under the influence of an external magnetic field gradient. For each of the system coordinates, the analytical integration with respect to time ( $t$ ) of this equation yields the microrobot velocity along its trajectory.

$$\vec{u}_p^{i+1} = \vec{u}_f^i + e^{-\frac{\Delta t}{\tau_p}} (\vec{u}_p^i - \vec{u}_f^i) - \tau_p \left( e^{-\frac{\Delta t}{\tau_p}} - 1 \right) \left[ \frac{\vec{g}(\rho_p - \rho_f)}{\rho_p} + \frac{V_p \cdot \nabla \vec{B} \cdot M_s}{m_p} \right] \quad (7)$$

where  $i$  is the current iteration of the calculations. As the microrobot velocity is the derivative of the microrobot position with respect to time,  $\vec{u}_p = \frac{d\vec{x}_p}{dt}$ , we can obtain the microrobot trajectory by replacing  $\vec{u}_p$  in Equation (7) by its derivative form, followed by its analytical integration with respect to time, yielding

$$\vec{x}_p^{i+1} = \vec{x}_p^i + t \left[ \vec{u}_f^i + \tau_p \left[ \frac{\vec{g}(\rho_p - \rho_f)}{\rho_p} + \frac{V_p \cdot \nabla \vec{B} \cdot M_s}{m_p} \right] \right] + \tau_p \left( 1 - e^{-\frac{t}{\tau_p}} \right) \left[ \vec{u}_p^i - \vec{u}_f^i - \tau_p \left[ \frac{\vec{g}(\rho_p - \rho_f)}{\rho_p} + \frac{V_p \cdot \nabla \vec{B} \cdot M_s}{m_p} \right] \right] \quad (8)$$

The microrobot trajectory is then obtained by iterating between Equations (7) and (8), for a time step  $\Delta t = 10^{-5} \cdot (u_p^i + u_f^i)^{-1}$ . The value  $10^{-6}$  was found to be adequate to accurately compute the microrobot trajectory over time, with smaller values yielding similar trajectories.

At every time step, the magnetic gradient needed to navigate the microrobot between its current position and the next target (i.e., one of the intermediate targets or the outlet) can be obtained by rearranging Equation (8) to isolate  $\nabla \vec{B}$ .

$$\nabla \vec{B} = \frac{\vec{d} - \vec{u}_f \cdot t - \vec{u}_p \cdot \tau_p + \vec{u}_f \cdot \tau_p + \tau_p \cdot e^{-\frac{t}{\tau_p}} (\vec{u}_p - \vec{u}_f) + \tau_p \cdot \frac{\vec{g}(\rho_p - \rho_f)}{\rho_p} \cdot \left( \tau_p - t - \tau_p \cdot e^{-\frac{t}{\tau_p}} \right)}{\frac{V_p \cdot M_s}{m_p} \cdot \tau_p \cdot \left( t - \tau_p + \tau_p \cdot e^{-\frac{t}{\tau_p}} \right)} \quad (9)$$

where  $\vec{d} = \vec{x}_p^{i+1} - \vec{x}_p^i$  is the distance to the next target, and  $t = \|\vec{d}\| \cdot \|\vec{u}_f\|^{-1}$  is the estimated time over which the microrobot will move between its current position and the next target. In this calculation, the microrobot was assumed to move with the velocity of the blood prevailing at its position, at every time instant.

At every iteration of the microrobot trajectory calculation, the magnetic gradient  $\nabla \vec{B}$  obtained by Equation (9) was used in Equation (7) to compute the microrobot velocity and in Equation (8) to compute the next microrobot position. This iterative process continued until the microrobot reached one of the bifurcation outlets.

## 2.4. Validation

To validate the flow prediction, the velocity profile and the fluid viscosity obtained with the present numerical approach at three different locations along the artery (i.e., inlet, halfway of the artery length, and three-quarters of the artery length) were compared with the analytical solutions of Equation (1) and (2),<sup>[44]</sup> respectively (Figure S4, Supporting Information, left and middle plots). The numerically predicted viscosity was also compared with measurement of various experimental works<sup>[71–74]</sup> (Figure S4, middle plot). The results of Figure S4 confirmed that the predicted flow was fully developed and showed a very good agreement between the obtained velocity and viscosity (hollow circles in Figure S4) and the corresponding analytical solutions and experimental data. That showed that the numerical approach developed in this work was valid and could be used to predict the flow in vascular structures.

To validate the motion and magnetic manipulation of the microrobots described by Equation (6), we did two different comparisons. In the first, we numerically replicated the work of Haverkort et al.<sup>[75]</sup> and compared the results obtained with our modeling approach with those in the mentioned work.

For the purpose, microrobots of different sizes (0.05–2  $\mu\text{m}$ ) were injected into a 90° bended tube where blood flowed at 0.10  $\text{m s}^{-1}$ , and a current-carrying wire, placed in the vicinity of the tube, generated a magnetic field to capture the injected microrobots. Figure S4 shows the capture efficiency predicted using our model and that reported in the mentioned work, as a function of the size of the injected microrobots. The agreement between both results indicated that the present numerical approach could be used to predict the magnetic force and the associated effect over the trajectory of microrobots injected into flows.

In the second comparison, we ran a series of in vitro experiments considering a bifurcation like that of the present work, for 32 different experimental conditions involving changes in flow velocity and magnetic gradient magnitudes (see Supporting Information for more details).

For each experimental condition, a polymeric sphere with ferromagnetic behavior and diameter of 1.4 mm was injected into a 5 mm-diameter bifurcation (Figure S5, Supporting Information) with flowing water. As in the present work, a magnetic gradient was used to steer the sphere toward a desired outlet. Four different flow velocities and eight magnetic gradient magnitudes (Table S1, Supporting Information) were combined following a full factorial design-of-experiments approach, where every

possible combination generated an independent experimental condition that was repeated 20 times, for a total of 640 experiments (i.e., 4 flow velocities  $\times$  8 magnetic gradient values  $\times$  20 repetitions). To replicate the in vitro experiments, a 3D model of the bifurcation was prepared, with mesh independence tests and validation of the flow calculations done as described in Section 2.3 and 2.4. The sphere motion and trajectory along the bifurcation were calculated by iterating Equation (7) and (8). At each iteration (and thus position of the sphere), the magnetic field and the magnetic field gradient data measured in the experiments (Table S1, Supporting Information) were used to calculate the sphere magnetization (Figure S6, Supporting Information) and the resulting magnetic force acting on the sphere (Equation (3)). For both the experiments and the corresponding simulations, we calculated the navigation success as the ratio between the number of polymeric spheres reaching the desired outlet and the total number of spheres entering the bifurcation (for both cases considering 20 spheres). Figure S7 shows the comparison between the navigation success observed in the experiments and that predicted by our model. The agreement between both results indicated that the modeling approach considered in this work could be used to predict the magnetic force and the associated effect over the trajectory of microrobots navigated through bifurcations.

## 2.5. Cases Considered for the Numerical Simulations

To investigate how magnetic gradients can be leveraged to navigate microrobots along artery bifurcations, we considered variations in various parameters affecting the microrobot trajectory. We considered five microrobot diameters (50–1000  $\mu\text{m}$ ), to study sizes relevant for drug-delivery applications, and that required different magnetic gradients for navigation. We considered the geometries of three cerebral arteries where most clots are observed (ACA, PCA, and MCA), considering five maximum blood velocities (0.25–0.65  $\text{m s}^{-1}$ ), in line with the ranges reported for healthy individuals. Moreover, we considered five entrance positions for the microrobots defined along the diameter of the inlet, as well as 16 different combinations of intermediate target positions (from  $-1D+1D$  to  $-4D+4D$ ). The values for each parameter (Table 2) were combined following a full factorial design-of-experiments approach, where each possible combination of the different parameters generated a simulation scenario. This resulted in a total of 6000 simulation scenarios (i.e., 5 microrobot diameters  $\times$  3 artery geometries  $\times$  5 blood flow velocities  $\times$  5 microrobot entrance positions  $\times$  16 target positions), which allowed studying the effects of each parameter over the microrobot trajectories and magnetic gradients required for successful navigation.

## 3. Results and Discussion

### 3.1. Microrobot Trajectory and Magnetic Gradients

We start by focusing on a simulation scenario describing the navigation of a 500  $\mu\text{m}$  microrobot released from the center position of the inlet of the anterior cerebral artery, for a maximum blood velocity of 0.45  $\text{m s}^{-1}$  and intermediate targets located at  $-2D+2D$  relative to the position of flow splitting, to analyze the microrobot

**Table 2.** Parameters considered in this work that were combined in a full-factorial design of experiments to produce 6000 different simulation scenarios.

microrobot diameter [ $\mu\text{m}$ ]	blood velocity [ $\text{m s}^{-1}$ ]	entrance position	upstream target	downstream target	artery
50	0.25	top wall	−1D	+1D	ACA
100	0.35	mid-top-center	−2D	+2D	MCA
250	0.45	center	−3D	+3D	PCA
500	0.55	mid-bot-center	−4D	+4D	
1000	0.65	bottom wall	−	−	

trajectory and the magnetic gradient required to navigate it through the bifurcation. **Figure 2** shows the microrobot trajectory, and the required magnetic gradient decomposed into the direction of the azimuthal angle (i.e., direction on the XY-plane) and the gradient magnitude, to enable a close inspection of the effect of the navigation parameters (i.e., direction and magnitude of the magnetic gradient).

The microrobot is successfully navigated to the desired outlet, with its trajectory following a smooth path from the inlet to the intermediate targets and to the outlet. In its motion toward the upstream target (first red circle in **Figure 2**), the microrobot moves along the length of the main artery (x-direction), and a small distance perpendicularly to the main flow (y-direction). While the microrobot motion along the x-direction is induced by the drag force of the blood flow, the motion along the y-direction must be induced by the application of an external force. Thus, the magnetic gradient points “upwards” in the y-direction (e.g.,  $x = 5 \text{ mm}$  in **Figure 2**) to induce a magnetic force that accelerates the microrobot toward the upstream target. As the microrobot moves along the bifurcation, the direction of the magnetic gradient changes to induce the deceleration (e.g.,  $x = 17 \text{ mm}$  in **Figure 2**), or acceleration (e.g.,  $x = 24 \text{ mm}$  in **Figure 2**) needed for the microrobot to reach each targets’ x- and y-positions at the same time.

The plot on the right side in **Figure 2** shows that the magnitude of the required magnetic gradient is very different depending on the position of the microrobots relative to the intermediate targets. The required magnetic gradients are lower between the

inlet and the upstream target (G1 region, **Figure 1**), higher between the upstream and the downstream targets (G2 region, **Figure 1**), and again lower between the downstream target and the outlet (G3 region, **Figure 1**). This pattern of variation indicates that it is useful to analyze the required magnetic gradients separately in each of these regions of the bifurcation (i.e., regions G1, G2, and G3, **Figure 1**), as the associated averages are a better representation of the original data.

That the magnetic gradients are higher in the G2 region is not surprising, because that is where the microrobot trajectory must be corrected toward the second intermediate target, over a relatively small distance (i.e., the distance between the targets upstream and downstream of the bifurcation). It is this dynamic variation of the magnetic gradient that allows for the desired navigation of the microrobots along the bifurcations.

### 3.2. Effect of the Parameters on the Magnetic Gradient

Here we study the influence of the different parameters on the magnetic gradients that navigate the microrobots along the artery bifurcations. The effect of each parameter on the microrobot trajectory, magnetic gradient direction, and magnetic gradient magnitude is shown in **Figure 3** for the anterior cerebral artery, where each parameter being considered (e.g., microrobot diameter) is varied for constant values of the others (i.e., diameter of  $500 \mu\text{m}$ , blood velocity of  $0.45 \text{ m s}^{-1}$ , entrance position at the center, and intermediate placed 2D upstream and downstream). The results of the variations are highlighted in different tints of blue, consistent across the three plots of trajectory, gradient direction, and gradient magnitude. The most relevant aspect that can be observed from **Figure 3** is that the magnitude in the G1 and G3 regions remains approximately constant across all scenarios, while the magnitude in the G2 region varies significantly between parameters.

Microrobots with different diameters require different magnetic gradients to be navigated along similar trajectories (**Figure 3**, top charts). For instance, an increase in the microrobot diameter from 50 to  $1000 \mu\text{m}$  decreases the G2 maximum magnitude from 11 to  $0.5 \text{ T m}^{-1}$ , a value more than 20 times lower, while still successfully navigating the microrobot. This decrease in the magnetic gradient magnitude is related to the effect of the

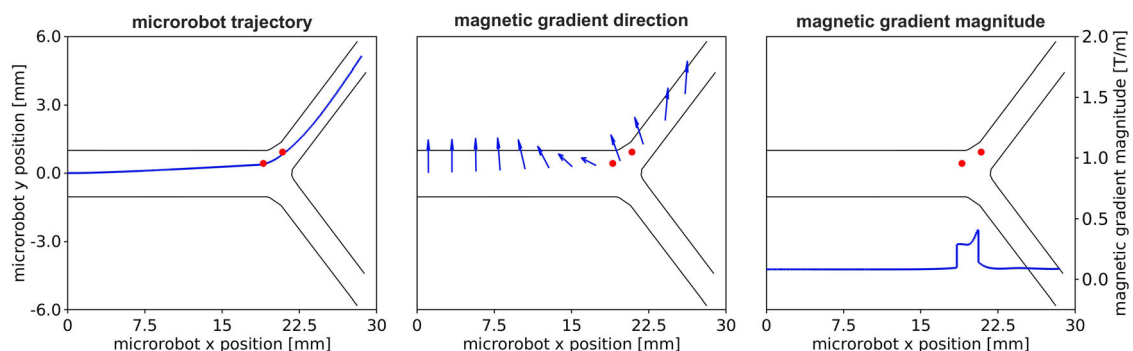


**Figure 2.** Microrobot trajectory along the bifurcation (top view of the XY-plane) and required magnetic gradient decomposed into the direction of the azimuthal angle (represented by the arrows) and gradient magnitude, for a  $500 \mu\text{m}$  microrobot released from the center position of the inlet of the anterior cerebral artery, for a maximum blood flow of  $0.45 \text{ m s}^{-1}$  and intermediate targets (red circles) placed at  $-2\text{D}+2\text{D}$  relative to the position of flow splitting.

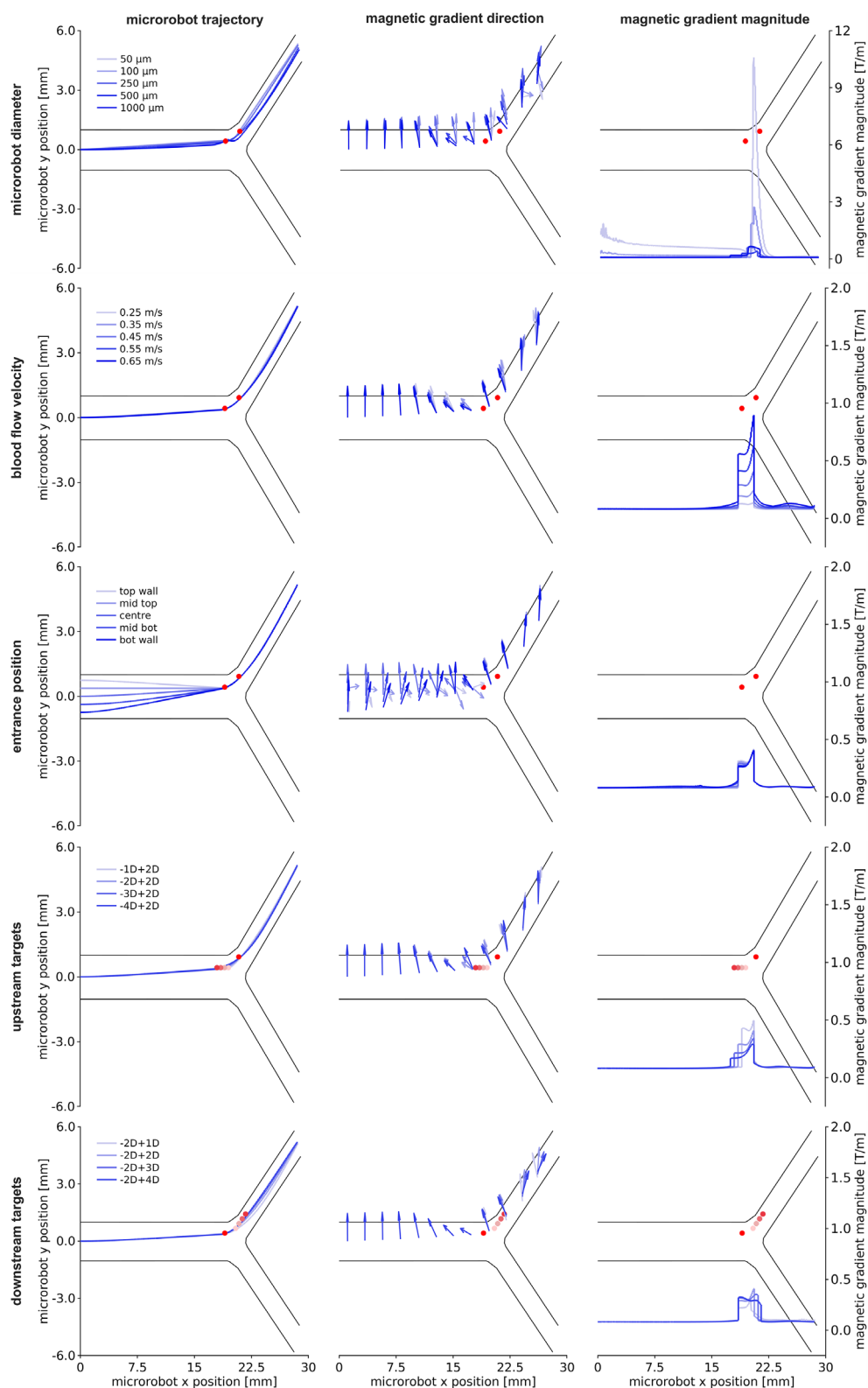


**Figure 3.** Effect of microrobot diameter, blood velocity, entrance position of the microrobot, and position of the intermediate targets, on the microrobot trajectory, magnetic gradient direction, and magnetic gradient magnitude for the anterior cerebral artery model. Within each row, each parameter is changed for constant values of the other parameters (e.g., diameter of 500  $\mu\text{m}$ , blood velocity of 0.45  $\text{m s}^{-1}$ , entrance position at the center of the artery, and intermediate targets placed 2D upstream and downstream the flow division). The red dots represent the upstream and downstream targets.



microrobot diameter in the drag and magnetic forces (Equation (6)). The drag force is dependent on the microrobot surface area, whereas the magnetic force is dependent on the microrobot volume. Thus, increasing the microrobot diameter increases the relevance of magnetic forces (depending on volume) relative to the drag forces (dependent on surface area), because of the increasing volume-to-surface-area ratio of the microrobots ( $=d_p/6$ ). This is convenient because the navigation of larger microrobots requires lower magnetic gradients and thus smaller/less powerful electromagnetic systems. Moreover, larger microrobots can carry higher doses of therapeutic agents which is interesting for drug delivery applications.<sup>[28–30]</sup> The choice of microrobot diameter should thus be weighted based on the available magnetic control system and the desired drug loading capacity.

Increasing the blood flow velocity has a very small effect over the microrobot trajectory and gradient direction, but a noticeable effect over the required magnetic gradients (Figure 3, 2nd row charts). Increasing the maximum velocity from 0.25 to 0.65 m s<sup>−1</sup> increased the G2 maximum magnitude from 0.15 to 0.90 T m<sup>−1</sup>, a sixfold increase, because correcting the trajectory of a microrobot moving faster requires higher magnetic forces. Thus, the magnetic gradients used for microrobot navigation should be adjusted depending on the flow velocity, knowing that higher flow velocities should require stronger magnetic gradients.

The different entrance positions of the microrobot into the bifurcation only have a noticeable effect on the direction of the magnetic gradient since the trajectory of the microrobot in all five scenarios converges, as required, to the upstream target (Figure 3, third-row charts). As expected, the required magnetic gradient points upward when the microrobot is released from near the bottom wall, and downward when it is released from near the top wall. For these scenarios, the maximum G2 magnitude remains constant around 0.4 T m<sup>−1</sup>. Thus, the entrance position of the microrobot does not have a meaningful impact on the magnetic gradients required to navigate the microrobots.

When varying the position of the intermediate targets (Figure 3, 4–5th row charts), as the upstream target gets closer to the point of flow division (i.e., from −4D to −1D), the maximum magnetic gradient increases slightly from 0.3 to 0.5 T m<sup>−1</sup>. Similarly, as the downstream target gets farther from the point of flow division (i.e., from +1D to +4D), the maximum magnetic gradient decreases slightly, from 0.4 to 0.3 T m<sup>−1</sup>. Given the different absolute positions of the different targets, the paths defined for the microrobot will have different lengths, which results in different instants at which the magnetic gradient must change the microrobot direction. Overall, the placement of the intermediate targets around the point of flow division has a small effect on the microrobot trajectory and on the magnetic gradient necessary for a successful navigation.

### 3.3. Maps for the Magnetic Gradients Magnitude

When computing the results of Figure 3, the required magnetic gradients were calculated considering the position and velocity of the microrobot at every time step, and the blood velocity prevailing in each position of the bifurcation. Therefore, this requires knowledge of the position and velocity of the microrobots at every time step of the calculation. Although accessing this data are

straightforward in numerical simulation, that may not be the case in a real clinical scenario, where imaging techniques (e.g., angiography) would have to be used at very high frequencies, thus repeatedly exposing the patient to radiation. Yet, the fact that the magnetic gradient required to navigate the microrobots varied almost only in the G2 region, with the gradients in the G1 and G3 regions being almost constant (Figure 3), indicates that one may not need to compute the gradients at every step, because the average values in each of the mentioned G1, G2, and G3 regions may be a good representation for the “instantaneous” gradient data. For that reason, we have computed the average magnetic gradient in the G1, G2, and G3 regions, for each of the 6000 simulation scenarios considered in this work, and generated plots like those of Figure 4 (and Figure S8–S21, Supporting Information) to show the resulting data as a function of various parameters (i.e., microrobot diameter, blood flow velocity, entrance position, and target position; a spreadsheet with the raw data is available in the Supporting Information). Figure 4 shows the average gradients in the G1, G2, and G3 regions together with the number of expected collisions, as a function of the upstream and downstream target position, the microrobot entrance position and the microrobot diameter, for a given artery geometry and blood flow. This type of plot offers quantitative information on the average gradients needed to steer the microrobots along the bifurcation, and on whether wall collisions are to be expected. Based on the data in this figure, a user wishing to navigate a 1000 μm microrobot along the bifurcation with the lowest G2 gradient and number of wall collisions, would know that he should place the intermediate targets at −1D+1D or −1D+2D position (two left plots in first row of Figure 4) and use G2 gradients of 0.4–0.6 T m<sup>−1</sup>. These results are in line with the results obtained in the experimental work of Belharet et al.<sup>[76]</sup> which reported magnetic gradients of 0.1–0.4 T m<sup>−1</sup> for a 500 μm spherical particle.

### 3.4. Analysis of the Obtained Magnetic Gradients (Magnitude and Angle)

The maps described in the previous section compile the average magnetic gradients in the G1, G2, and G3 regions for all the 6000 simulation cases and provide useful quantitative information on the magnitude range for different scenarios. Yet, they still provide limited information on how the gradients vary across all the cases for a given parameter value (e.g., blood velocity of 0.35 m s<sup>−1</sup>, or a microrobot diameter of 250 μm). To further study these variations, the average data in the G1, G2, and G3 regions were statistically analyzed using boxplots, specifically regarding the magnitude and angle of the magnetic gradient. An example of this analysis is shown in Figure 5 for the G2 region, where the magnitude and angle values were grouped according to the different parameters of microrobot diameter (50–1000 μm), blood flow velocity (0.25–0.65 m s<sup>−1</sup>), entrance position (top wall to bottom wall), and intermediate targets position (−1D+1D to −4D+4D). The boxplots in each row of Figure 5 were generated for each of the parameters considered by choosing a given value (e.g., microrobot diameter of 50 μm) and grouping all the data obtained for that constant parameter value (e.g., from the 6000 simulation scenarios considered, there are 1200 for which the

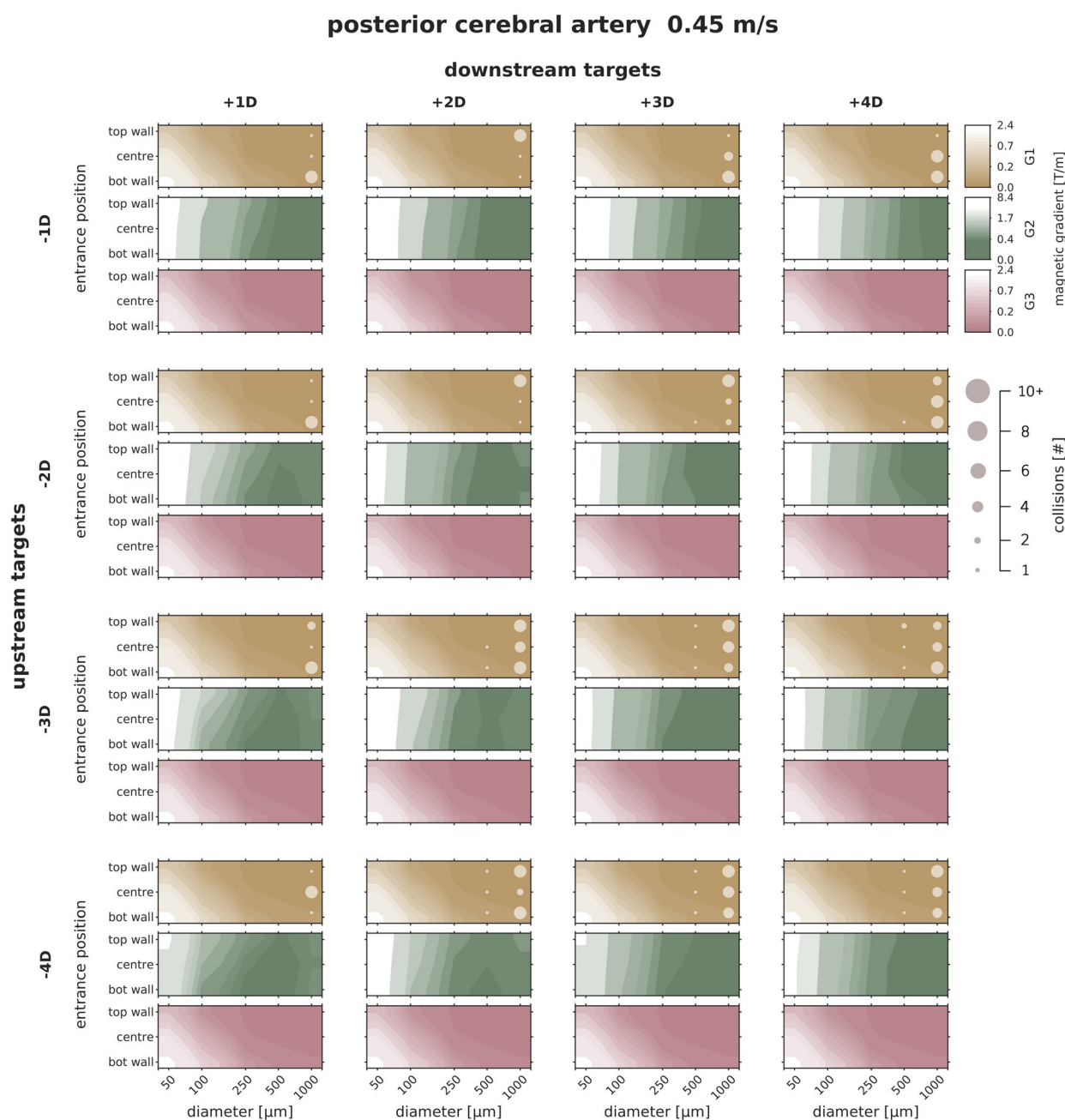


**Figure 4.** Maps of the magnetic gradient magnitude in the G1, G2, and G3 regions, and number of wall collisions, for microrobots with diameters of 50, 100, 250, 500, and 1000  $\mu\text{m}$ , released in the posterior cerebral artery at the top, center, and bottom positions, for intermediate target positions between  $-4\text{D}$  and  $+4\text{D}$  and maximum blood velocity of  $0.45 \text{ m s}^{-1}$ .

diameter is equal to  $50 \mu\text{m}$  since we analyzed five different diameter values). The blue rectangle represents the interquartile range that contains 50% of the data points. The bottom and top lines of the rectangle represent the lower and upper quartiles, which represent the values below and above which 25% of the data falls. The red line inside the rectangle represents the median value, and the black horizontal lines represent the minimum/maximum values that fall  $1.5\times$  the value of the interquartile range, below/above the lower/upper quartile. Finally, the red dots represent the outliers,

which are lower or higher than the minimum and maximum values, respectively.

These plots are useful to study the variability and skewness of the results of the different parameter values. For instance, when the rectangles of the boxplots are small, the interquartile range is narrow and the results have low variability, as 50% of the data points are contained between that range. Low variability suggests the gradients obtained in the different simulation scenarios are similar (meaning that the different values considered in the

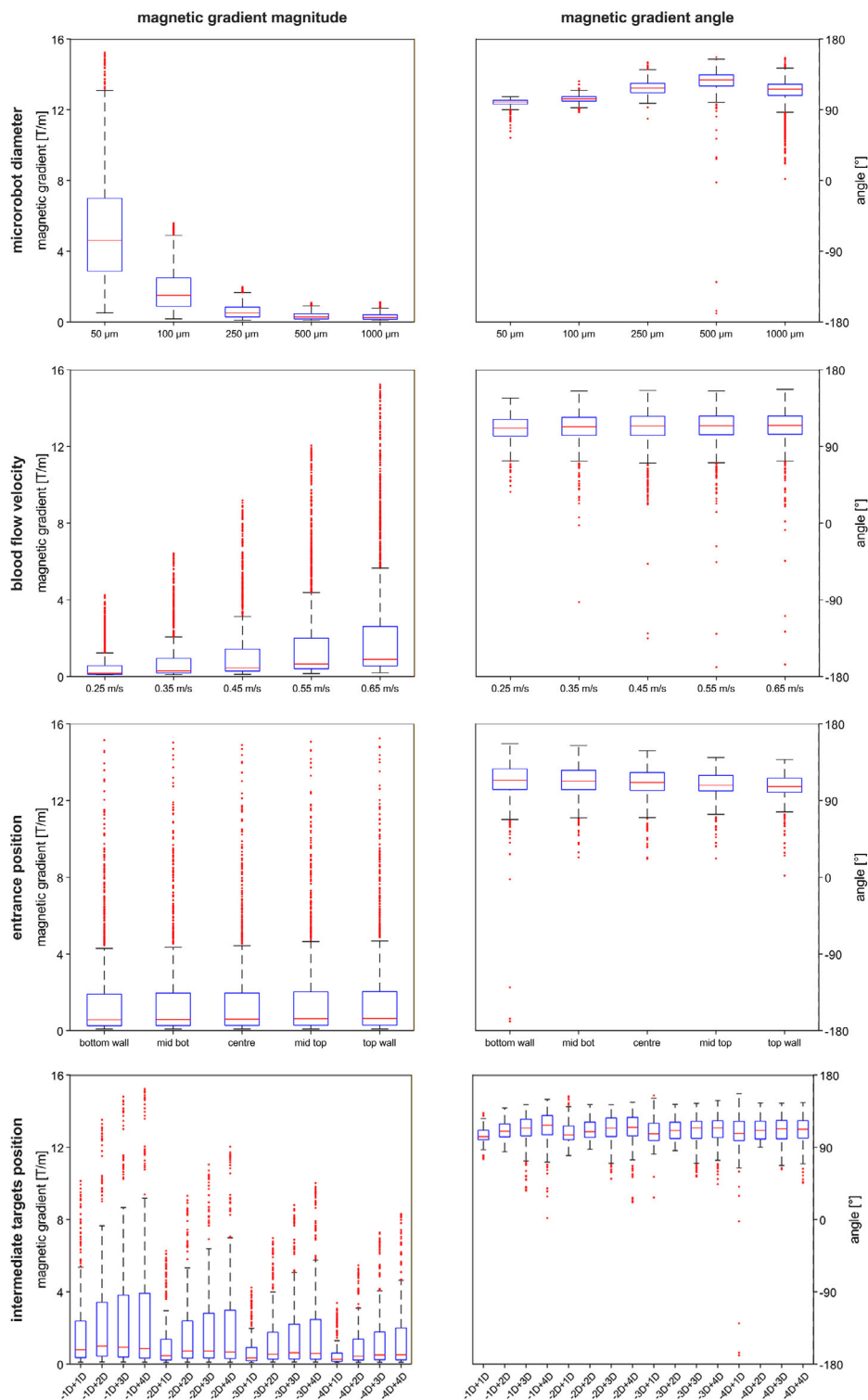


**Figure 5.** Boxplots for the G2 gradient (magnitude and azimuthal angle), grouped according to the values for the microrobot diameter (50–1000  $\mu\text{m}$ ), blood flow velocity (0.25–0.65  $\text{m s}^{-1}$ ), and intermediate targets position (−1D+1D to −4D+4D). The blue rectangle represents the interquartile range, which contains 50% of the data points; the bottom and top lines of the rectangle are the lower and upper quartiles, where 25% of the data points are below the lower quartile and 25% are above the upper quartile; the red line inside the rectangle represents the median value; the black horizontal lines represent the minimum/maximum values that fall 1.5 $\times$  the value of the interquartile range, below/above the lower/upper quartile; the red dots represent the outliers, which are lower or higher than the minimum and maximum values, respectively.

tested scenarios do not have a large footprint in the results). Additionally, when the interquartile range and median of two boxplots are similar, one can infer that the parameters considered in each of the two boxplots produce similar gradients.

When the diameter of the microrobot increases (Figure 5, first-row plots), there is a sharp decrease in the maximum, the interquartile range, and the median value of the G2 gradient, indicating that the microrobot diameter has a large footprint in the obtained gradients. Furthermore, that the median gradient has a distinctive value for each of the tested different diameters suggests that this parameter can be used to predict the gradient required for the microrobot navigation. Additionally, for diameters  $>250\text{ }\mu\text{m}$  all the results cluster around very small values, indicating low variability, thus similar magnetic gradients across all the scenarios with diameters  $>250\text{ }\mu\text{m}$ . On the other hand, the boxplots for the angle of the magnetic gradient in the G2 region (Figure 5, right plot in the first row) show that the results do not have distinctive median values for each of the diameters studied, with similar ranges and median values across all diameters. This shows that the G2 angle cannot be easily predicted based on the microrobot diameter, which is not surprising as the gradient direction is adjusted every time the microrobot must be accelerated/deaccelerated, as needed to change direction (between targets), or anytime it collides with the walls.

When analyzing the results for the blood velocity, entrance position, and target positions (Figure 5, 2nd–4th rows), we see that the corresponding boxplots exhibit high variability, high number of outliers, and no distinctive medians across the different values considered, both for the magnitude and the angle (left and right plots, Figure 5). This suggests that the median G2 magnitude and angle required for navigating the microrobot cannot be easily predicted based on the values of the blood velocity, entrance position, and target position. Additionally, the analysis of the boxplots for G2 (Figure 5) together with those for G1 and G3 (Figure S22 and S23, Supporting Information) indicates that the median angle data appear to cluster around  $90^\circ$  across all tested scenarios. This was expected because an angle of  $90^\circ$  corresponds to the direction perpendicular to the flow along the main artery, for which the microrobot motion will depend entirely on the applied magnetic gradient (the microrobot only moves perpendicular to the flow if a magnetic gradient applies a force in that direction).

### 3.5. Data-Driven Modeling to Generate Predictive Equation

Having analyzed in the previous section the variability of the data for the different parameters considered, we then turned our attention to the average median magnetic gradients obtained in the G1, G2, and G3 regions (Table 3). We focused on the data obtained for the minimum and maximum values of the five parameters considered in this work (i.e., microrobot diameter, blood flow, entrance position, and target positions), for assessing the relative importance of changes in each of the five parameters, over the required average G1–G3 values. The data in Table 3 highlights again the importance of the microrobot diameter on the magnitude of the required gradients, with the corresponding ratio between the minimum and maximum values of G1–G3 being consistently higher than the data obtained for all the other four parameters (Table 3). For instance, the median G1 magnitude value for the  $50\text{ }\mu\text{m}$  microrobot is 8.6 times bigger than that for the  $1000\text{ }\mu\text{m}$  microrobot, and the difference for G2 and G3 is even larger, sitting at 18.6 and 10.1 (Table 3, first row). In stark contrast, the mentioned differences for changes in blood flow, entrance position, and target positions, range between 0.2 and 1.0 (Table 3, 2nd–4th rows). This shows that the microrobot diameter has the largest footprint in the obtained gradient results and can, thus, be used as an input parameter in a data-driven modeling<sup>[77]</sup> approach for generating equations that can predict the median magnitude of G1, G2, and G3, based on the chosen microrobot diameter. Such equations are useful because they should eliminate the need for running new simulations for each new set of parameters, since they could be used to predict the required gradients without running any simulation. Figure 6 shows the second-order linear equations that were obtained using the least-squares method,<sup>[77]</sup> to predict the median G1, G2, and G3 values, as a function of the microrobot diameter.

After obtaining equations for predicting the required magnetic gradients in the G1, G2, and G3 regions, we checked if the predicted gradients would lead to successful navigation of the microrobot along the bifurcation. For this purpose, the entire set of 6000 simulation scenarios was resimulated, but now considering constant median values for G1, G2, and G3, given by the developed predictive equations, instead of calculating the magnetic gradient at every time step (as done in Section 3.1). Furthermore, in these new simulations, we set the gradient

**Table 3.** Median values of magnetic gradients [ $\text{T}\cdot\text{m}^{-1}$ ] in the G1, G2, and G3 regions, obtained for the maximum and minimum values of each parameter considered (diameter, blood velocity, entrance position, and target position), and ratio between the minimum and maximum values obtained.

parameter	minimum maximum	G1 [ $\text{T}\cdot\text{m}^{-1}$ ]	$\frac{G1_{\text{minimum}}}{G1_{\text{maximum}}}$	G2 [ $\text{T}\cdot\text{m}^{-1}$ ]	$\frac{G2_{\text{minimum}}}{G2_{\text{maximum}}}$	G3 [ $\text{T}\cdot\text{m}^{-1}$ ]	$\frac{G3_{\text{minimum}}}{G3_{\text{maximum}}}$
diameter [ $\mu\text{m}$ ]	50	0.7069	8.6	4.6098	18.6	0.9064	10.1
	1000	0.0822		0.2481		0.0901	
blood flow [ $\text{m s}^{-1}$ ]	0.25	0.0836	0.7	0.1936	0.2	0.0892	0.5
	0.65	0.1142		1.0169		0.1779	
entrance position	top wall	0.0922	0.7	0.6262	1.1	0.1257	1.0
	bottom wall	0.1378		0.5603		0.1270	
target positions	–4D	0.0933	1.0	0.4245	0.5	0.1269	1.0
	–1D	0.0920		0.8927		0.1211	



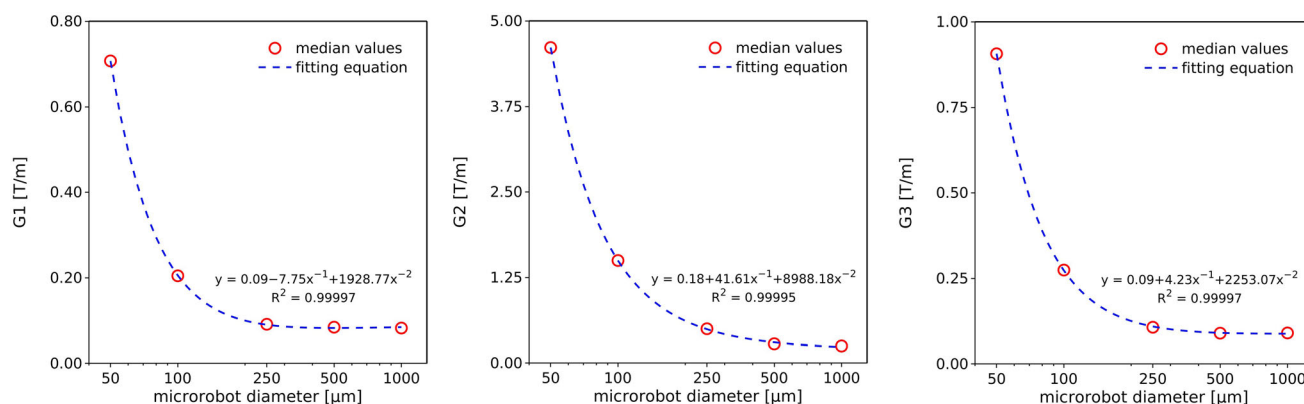


**Figure 6.** Median values of G1, G2, and G3 magnitude for each microrobot diameter and respective fitting equations obtained using the least-squares method.<sup>[77]</sup> The fitting equations can be used to predict the required G1–G3 values as a function of the microrobot diameter, consisting of magnetic material only (i.e., magnetic volume = microrobot volume) with magnetization equal to the saturation value (see Section 2.2.3). These equations can be adapted to other magnetic volume and magnetic saturation values by multiplying the coefficient terms obtained in this work by the ratio between the microrobot volume and the new magnetic volume, and the ratio between the saturation magnetization and the new magnetization value (see the applicable equations in Supporting Information).

azimuthal angle (i.e., the angle required to navigate the microrobot toward the top outlet) and the gradient polar angle (i.e., the angle required to compensate for the effect of gravity) to a constant value of 90°, because it is the angle around which the results clustered (as explained when analyzing Figure 5), but also because it is the angle at which the magnetic actuation is more efficient.

After rerunning the 6000 simulations, we conducted a similar analysis to that described in Section 3.4, and computed the navigation success as the ratio between the number of microrobots reaching the target branch and the total number of microrobots entering the bifurcation. When updating the magnetic gradient at every time step (dynamic method), the navigation success was 100% (meaning that, in all the 6000 scenarios, the microrobots were successfully navigated to the desired branch). When doing the navigation using the constant values of the G1–G3 gradients predicted by the developed predictive equations (constant method, Figure 6), the navigation success dropped to 94.6% (in 324 cases, the microrobot did not go to the desired branch). More importantly, the navigation was unsuccessful mostly for the smallest microrobots diameters (i.e., 50 and 100 μm), which is not particularly problematic because these diameters imply impractically large magnetic gradients, and because they are less interesting for drug delivery (because of the lower loads that can be transported in the microrobots). Furthermore, the navigation was not successful in some scenarios because the generated magnetic force was not sufficient to push the microrobot toward the top half of the bifurcation, or because collisions with the wall made the microrobot divert to the bottom outlet (Figure S24, Supporting Information). Nevertheless, these results are very interesting because they show that the median gradients obtained for G1, G2, and G3 can be used to successfully navigate microrobots for most of the tested diameters, in a wide range of scenarios.

Having assessed the navigation success when using constant values for the magnetic gradients in the G1–G3 regions, we then focused on checking the robustness of the developed predictive/

fitting equations (Figure 6). To this end, a new set of 6000 simulation cases was created using three new artery models (artery diameters of Table 1 increased by 0.2 mm), five new blood flow velocities, and five new microrobot diameters (Table 4), and different absolute values for the entrance position and the intermediate targets (as these two parameters vary with the microrobot diameter). These 6000 new scenarios were first simulated with the dynamic method to obtain the median gradient magnitude and then simulated again using the constant median gradient magnitude calculated by the fitting equations, to assess the success of the magnetic navigation.

We compare in Table 5 the new median G1–G3 values obtained via the dynamic method, with the G1–G3 values obtained via the fitting equations. The G1–G3 values obtained via the fitting equations underestimate the G1–G3 values obtained via the dynamic method, with average differences being 8.6% for G1, 17.1% for G2, and 10.4% for G3. The difference between the G1–G3 values obtained via the dynamic method and via the fitting equations is higher for the smaller microrobots (75 and 175 μm), because they imply the largest magnetic gradients due to the corresponding larger surface area to volume ratio of these microrobots (which increase the relevance of the drag force relative to the magnetic force). Nevertheless, after assessing the navigation success, we observed that the magnetic navigation was successful for 95.1% of the cases, with only 292 out of 6000 simulation scenarios having

**Table 4.** Parameter values for the new simulation scenarios.

microrobot diameter [μm]	blood flow velocity [m s <sup>-1</sup> ]	entrance position	upstream target	downstream target	artery
75	0.30	top wall	−1D	+1D	ACA
175	0.40	mid-top-center	−2D	+2D	MCA
375	0.50	center	−3D	+3D	PCA
650	0.60	mid-bot-center	−4D	+4D	
850	0.70	bottom wall			

**Table 5.** Expected and obtained G1/G2 values and their difference (%) for each new microrobot diameter.

		G1 (dynamic)	G1 (equation)	difference	G2 (dynamic)	G2 (equation)	difference	G3 (dynamic)	G3 (equation)	difference
microrobot diameter [ $\mu\text{m}$ ]	75	0.414	0.330	25.4	2.903	2.335	24.3%	0.531	0.434	22.4%
	175	0.118	0.109	8.2%	0.863	0.714	20.9%	0.159	0.139	14.2%
	375	0.088	0.083	6.1%	0.414	0.357	15.8%	0.098	0.095	3.9%
	650	0.085	0.083	2.8%	0.297	0.268	10.9%	0.094	0.089	5.6%
	850	0.084	0.084	0.3%	0.277	0.244	13.6%	0.093	0.088	5.7%

resulted in the microrobot going to the bottom outlet. This is a very positive indicator because it shows that, even with deviations between the expected and calculated values, the constant magnetic gradients obtained via the fitting equations are sufficient to navigate most microrobots to the desired branch/outlet.

The magnetic gradients predicted by our equations are also consistent with the gradients reported in several experimental works involving in vivo navigation. In the work of Martel and colleagues,<sup>[78]</sup> a 1.5 mm microrobot was navigated in the carotid artery of a swine. To this end, magnetic gradients generated by an MRI machine were used to steer the microrobot along different waypoints in the carotid artery without bifurcations. The magnetic gradients reported in that work ( $0.05 \text{ T m}^{-1}$ ) are in line with those obtained in our work for a 1 mm microrobot (median G1 value of  $0.08 \text{ T m}^{-1}$ , Table 3), with differences being likely related to the larger size of the microrobot and lower flow velocity used in the experiments (size of 1.5 vs. 1.0 mm in our work, and flow velocities up to  $0.13 \text{ m s}^{-1}$  vs.  $0.25\text{--}0.65 \text{ m s}^{-1}$  in our work; the required magnetic gradients decrease with increasing microrobot size and decreasing flow velocity, Table 3). Also, in the experimental study by Lalande et al.<sup>[79]</sup> a ferromagnetic bead with a diameter of 0.9 mm was magnetically navigated in the renal arteries of four rabbits, with successful steering at the bifurcating arteries being reported when imposing magnetic gradients up to  $0.5 \text{ T m}^{-1}$ . Such magnetic gradients are well in the range of the ones predicted in our study for a 1 mm microrobot (median G2 value of  $0.25 \text{ T m}^{-1}$ , Table 3). The fact that the ranges of magnetic gradients found in our work to be adequate for navigating microrobots along various bifurcations are consistent with those reported in different experimental studies is further an indicator of the validity of the predictive equations developed in this work.

## 4. Conclusions

We studied the navigation of microrobots in the blood flowing through representative cerebral bifurcations, for predicting the magnetic gradients needed to navigate the microrobots until the target locations. We numerically simulated the blood flow at different velocities for three cerebral arteries and calculated the microrobots trajectory and the magnetic gradient that would steer them along intermediate targets to the desired branch/outlet. When computing the magnetic gradients at every time step, we observed that all the microrobots were successfully navigated to the desired branch/outlet. We then analyzed the magnetic gradient in three regions of the bifurcations (G1, G2, and

G3), corresponding to the three paths defined by the intermediate targets. We examined the effect of microrobot diameter, artery geometry, blood velocity, injection point, and target locations, on the microrobot trajectory and magnetic gradients required to navigate them along the bifurcations. We saw that an increase in the microrobot diameter from 50 to  $1000 \mu\text{m}$  would decrease the maximum gradient by  $>20$  fold. In contrast, increasing the maximum velocity from  $0.25$  to  $0.65 \text{ m s}^{-1}$  increased the maximum gradient by sixfold, with the entrance position of the microrobot having a noticeable effect only on the direction of the magnetic gradient. The average magnetic gradients were compiled into maps providing quantitative information on the range of values needed for different scenarios. The analysis of the results showed that the microrobot diameter was the most relevant parameter for predicting the magnetic gradients required to magnetically navigate the microrobot. We then used a data-driven modeling approach for generating second-order linear equations predicting the median magnitude of G1–G3, as a function of the microrobot diameter. We tested the robustness of the developed fitting/predictive equations and observed that microrobots could be successfully navigated along the bifurcations in the vast majority ( $>95\%$ ) of the tested simulation scenarios. This confirmed the robustness of the developed equations and showed the usefulness of using constant magnetic gradients dependent on the microrobot diameter, to navigate the microrobots along vascular networks. The obtained results are important for guiding the development of magnetic navigation systems, with the developed maps and predictive equations offering easy-to-use data to inform the design, operation, and optimization of such navigation systems.

## Supporting Information

Supporting Information is available from the Wiley Online Library or from the author.

## Acknowledgements

Part of this work was supported by the European Union's H2020 research and innovation programme under grant agreement nos. 801464, 668786, and 952152, as well as by Horizon Europe research and innovation programme under grant agreement no. 101047081. T.S.M. and P.G.A. acknowledge the support by LA/P/0045/2020 (ALiCE), UIDB/00532/2020, and UIDP/00532/2020 (CEFT), funded by Portugal through FCT/MCTES (PIDDAC). J.P.L. also acknowledges the Agencia Estatal de Investigación (AEI) for the María de Maeztu, project no. CEX2021-001202-M, the grant PID2020-116612RB-C33 funded by MCIN/AEI/

10.13039/501100011033, and the Generalitat de Catalunya for the project 2021SGR 00270.

## Conflict of Interest

The authors declare no conflict of interest.

## Author Contributions

**Pedro G. Alves:** data curation (equal); formal analysis (equal); investigation (equal); methodology (equal); writing—original draft (equal); writing—review & editing (equal). **Maria Pinto:** investigation (equal); methodology (equal); project administration (supporting); visualization (equal); writing—original draft (equal); writing—review & editing (equal). **Rosa Moreira:** funding acquisition (equal); investigation (equal); methodology (equal); project administration (supporting); visualization (equal); writing—original draft (equal); writing—review & editing (equal). **Derick Sivakumaran:** data curation (supporting); formal analysis (supporting); methodology (supporting); validation (equal); visualization (equal); writing—original draft (equal); writing—review & editing (equal). **Fabian Landers:** data curation (supporting); formal analysis (supporting); methodology (supporting); validation (equal); visualization (equal); writing—original draft (equal); writing—review & editing (equal). **Maria Guix:** investigation (supporting); methodology (supporting); writing—original draft (supporting); writing—review & editing (supporting). **Bradley J. Nelson:** conceptualization (supporting); funding acquisition (supporting); investigation (supporting); methodology (supporting); writing—original draft (supporting); writing—review & editing (supporting). **Andreas D. Flouris:** investigation (supporting); methodology (supporting); writing—original draft (supporting); writing—review & editing (supporting). **Salvador Pané:** conceptualization (equal); funding acquisition (equal); investigation (equal); methodology (equal); writing—original draft (equal); writing—review & editing (equal). **Josep Puigmartí-Luis:** conceptualization (equal); funding acquisition (equal); investigation (equal); methodology (equal); supervision (supporting); writing—original draft (equal); writing—review & editing (equal). **Tiago S. Mayor:** conceptualization (equal); formal analysis (equal); investigation (equal); methodology (equal); supervision (lead); visualization (equal); writing—original draft (equal); writing—review & editing (equal).

## Data Availability Statement

The data that support the findings of this study are available in the supplementary material of this article.

## Keywords

blood flow simulations, cerebral bifurcations, drug deliveries, magnetic manipulations, microrobots, numerical simulations

Received: November 18, 2024

Revised: April 18, 2025

Published online:

- [1] Global Burden of Disease Study 2019 (GBD 2019) Data Resources I GHDx.
- [2] A. Moussaddy, A. M. Demchuk, M. D. Hill, *Neuropharmacology* **2018**, 134, 272.
- [3] J. M. Wardlaw, V. Murray, E. Berge, G. J. del Zoppo, *Cochrane Database Syst. Rev.* **2014**, 2014, CD000213.
- [4] W. J. Powers, A. A. Rabinstein, T. Ackerson, O. M. Adeoye, N. C. Bambakidis, K. Becker, J. Biller, M. Brown, B. M. Demaerschalk,

- B. Hoh, E. C. Jauch, C. S. Kidwell, T. M. Leslie-Mazwi, B. Ovbiagele, P. A. Scott, K. N. Sheth, A. M. Southerland, D. V. Summers, D. L. Tirschwell, *Stroke* **2019**, 50, e344.
- [5] N. H. S. England, *Clinical Commissioning Policy: Mechanical Thrombectomy for Acute Ischaemic Stroke (All Ages)*, NHS England **2018**, p. 20.
- [6] S. R. Messé, L. H. Schwamm, *Neurology* **2017**, 88, 1383.
- [7] J. Díaz-Pérez, G. Parrilla, M. Espinosa De Rueda, J. M. Cabrera-Maqueda, B. García-Villalba, M. T. Alba-Isasi, A. Morales, J. Zamarro, *Cerebrovasc. Dis.* **2018**, 46, 130.
- [8] D. Jang, J. Jeong, H. Song, S. K. Chung, *J. Micromech. Microeng.* **2019**, 29, 053002.
- [9] P. Erkoç, I. C. Yasa, H. Ceylan, O. Yasa, Y. Alapan, M. Sitti, *Adv. Ther.* **2019**, 2, 1800064.
- [10] H. Ceylan, I. C. Yasa, U. Kilic, W. Hu, M. Sitti, *Prog. Biomed. Eng.* **2019**, 1, 012002.
- [11] B. J. Nelson, I. K. Kaliakatsos, J. J. Abbott, *Annu. Rev. Biomed. Eng.* **2010**, 12, 55.
- [12] F. Soto, R. Chrostowski, *Front. Bioeng. Biotechnol.* **2018**, 6, 170.
- [13] M. Wautelet, *Eur. J. Phys.* **2001**, 22, 601.
- [14] E. M. Purcell, *Am. J. Phys.* **1977**, 45, 3.
- [15] C. Chautems, B. Zeydan, S. Charreyron, G. Chatzipirpiridis, S. Pané, B. J. Nelson, *Eur. J. Cardio-Thoracic Surg.* **2017**, 51, ezw432.
- [16] E. B. Steager, M. Selman Sakar, C. Magee, M. Kennedy, A. Cowley, V. Kumar, *Int. J. Rob. Res.* **2013**, 32, 346.
- [17] L. Zhang, J. J. Abbott, L. Dong, B. E. Kratochvil, D. Bell, B. J. Nelson, *Appl. Phys. Lett.* **2009**, 94, 13.
- [18] M. A. Zeeshan, R. Grisch, E. Pellicer, K. M. Sivaraman, K. E. Peyer, J. Sort, B. Özkale, M. S. Sakar, B. J. Nelson, S. Pané, *Small* **2014**, 10, 1284.
- [19] R. Pieters, H. W. Tung, S. Charreyron, D. F. Sargent, B. J. Nelson, in *Proc. IEEE Int. Conf. Robotics and Automation 2015*, Seattle, WA, US, June **2015** p. 4042.
- [20] D. R. Frutiger, K. Vollmers, B. E. Kratochvil, B. J. Nelson, *Int. J. Rob. Res.* **2010**, 29, 613.
- [21] C. Pawashe, S. Floyd, M. Sitti, *Int. J. Rob. Res.* **2009**, 28, 1077.
- [22] H. Torlakcik, S. Sevim, P. Alves, M. Mattmann, J. Llacer-Wintle, M. Pinto, R. Moreira, A. D. Flouris, F. C. Landers, X. Z. Chen, J. Puigmartí-Luis, Q. Boehler, T. S. Mayor, M. Kim, B. J. Nelson, S. Pané, *Adv. Sci.* **2024**, 11, 2404061.
- [23] S. Kenjereš, B. W. Righolt, *Int. J. Heat Fluid Flow* **2012**, 35, 68.
- [24] E. M. Cherry, P. G. Maxim, J. K. Eaton, *Med. Phys.* **2010**, 37, 175.
- [25] S. Bose, M. Banerjee, *J. Magn. Magn. Mater.* **2015**, 385, 32.
- [26] M. M. Larimi, A. Ramiar, A. A. Ranjbar, *J. Magn. Magn. Mater.* **2014**, 362, 58.
- [27] O. Pourmehran, T. B. Gorji, M. Gorji-Bandpy, *Biomech. Model. Mechanobiol.* **2016**, 15, 1355.
- [28] K. Trzeciak, A. Chotera-ouda, I. I. Bak-sypien, M. J. Potrzebowski, *Pharmaceutics* **2021**, 13, 950.
- [29] S. Shen, Y. Wu, Y. Liu, D. Wu, *Int. J. Nanomed.* **2017**, 12, 4085.
- [30] M. Li, J. Wu, D. Lin, J. Yang, N. Jiao, Y. Wang, L. Liu, *Acta Biomater.* **2022**, 154, 443.
- [31] D. Jiles, *Introduction to Magnetism and Magnetic Materials*, 3rd ed., CRC Press, Boca Raton **2015**.
- [32] M. A. Davison, B. Ouyang, K. M. Keppetipola, M. Chen, *J. Neurointerv. Surg.* **2018**, 10, 949.
- [33] P. McMeekin, P. White, M. A. James, C. I. Price, D. Flynn, G. A. Ford, *Eur. Stroke J.* **2017**, 2, 319.
- [34] J. H. Badhiwala, F. Nassiri, W. Alhazzani, M. H. Selim, F. Farrokhyar, J. Spears, A. V. Kulkarni, S. Singh, A. Alqahtani, B. Rochwerg, M. Alshahrani, N. K. Murty, A. Alhazzani, B. Yarascavitch, K. Reddy, O. O. Zaidat, S. A. Almenawer, *JAMA* **2015**, 314, 1832.
- [35] A. T. Rai, A. E. Seldon, S. Boo, P. S. Link, J. R. Domico, A. R. Tarabishy, N. Lucke-Wold, J. S. Carpenter, *J. Neurointerv. Surg.* **2017**, 9, 722.

- [36] K. Cieslicki, D. Ciesla, *J. Biomech.* **2005**, *38*, 2302.
- [37] E. Tarasów, A. Abdulwahed Saleh Ali, A. Lewszuk, J. Walecki, *Med. Sci. Monit.* **2007**, *13*, 65.
- [38] R. Valvita, B. Sadi, *J. Neurol. Neurol. Sci. Disord.* **2019**, *5*, 052.
- [39] P. Mouches, N. D. Forkert, *Sci. Data* **2019**, *6*, 29.
- [40] J. Alastruey, K. H. Parker, J. Peiró, S. M. Byrd, S. J. Sherwin, *J. Biomech.* **2007**, *40*, 1794.
- [41] C. D. Murray, *J. Gen. Physiol.* **1931**, *14*, 445.
- [42] B. M. Koeppen, B. A. Stanton, *Berne & Levy Physiology*, 7th ed., Elsevier, Philadelphia **2017**.
- [43] L. Waite, J. Fine, *Applied Biofluid Mechanics*, 1st ed., McGraw-Hill, New York **2007**.
- [44] R. P. Chhabra, J. F. Richardson, *Non-Newtonian Flow in the Process Industries*, Butterworth-Heinemann, Oxford **1999**.
- [45] L. Campo-Deano, M. S. N. Oliveira, F. T. Pinho, *Appl. Mech. Rev.* **2015**, *7(3)*, 34102.
- [46] I. Husain, F. Labropulu, C. Langdon, J. Schwark, *J. Mech. Behav. Mater.* **2020**, *21*, 147.
- [47] L. Chen, *Hemodynamics in the Cerebral Circulation: Numerical Studies and Experimental Investigation* (PhD diss., Nanyang Technological University, Singapore, **2005**), <https://dr.ntu.edu.sg/server/api/core/bitstreams/bd652b3c-591d-4393-bda6-be8c88dd3aef/content>.
- [48] B. Hillen, B. A. H. Drinkenburg, H. W. Hoogstraten, L. Post, *J. Biomech.* **1988**, *21*, 807.
- [49] P. Fahy, P. McCarthy, S. Sultan, N. Hynes, P. Delassus, L. Morris, *Ann. Biomed. Eng.* **2014**, *42*, 123.
- [50] T. Fukushima, T. Homma, T. Azuma, K. Harakawa, *Biorheology* **1987**, *24*, 3.
- [51] C. Karmonik, O. Diaz, R. Klucznik, R. G. Grossman, Y. J. Zhang, G. Britz, N. Lv, Q. Huang, *J. Neurointerv. Surg.* **2015**, *7*, 367.
- [52] J. Mikhal, C. H., B. J., *Aneurysm*, InTech (Japan) **2012**.
- [53] C. S. Kim, C. Kiri, D. Kwak, T. David, *J. Biomech. Eng.* **2006**, *128*, 194.
- [54] A. D. Malcolm, M. R. Roach, *Stroke* **1979**, *10*, 335.
- [55] S. J. Cho, Y. H. Sohn, G. W. Kim, J. S. Kim, *J. Neurol. Sci.* **1997**, *150*, 77.
- [56] R. E. Kelley, J. Y. Chang, N. J. Scheinman, B. E. Levin, R. C. Duncan, S. C. Lee, *Stroke* **1992**, *23*, 9.
- [57] S. Demirkaya, K. Uluc, S. Bek, O. Vural, *Tohoku J. Exp. Med.* **2008**, *214*, 145.
- [58] T. S. Lyngeraa, L. M. Pedersen, T. Mantoni, B. Belhage, L. S. Rasmussen, J. J. van Lieshout, F. C. Pott, *Scand. J. Med. Sci. Sports* **2013**, *23*, 32.
- [59] C. T. Crowe, J. D. Schwarzkopf, M. Sommerfeld, Y. Tsuji, *Multiphase Flows with Droplets and Particles*, 2nd ed., Taylor & Francis Group (Boca Raton) **2012**.
- [60] A. Sinha, R. Ganguly, K. A. De, K. I. Puri, *Phys. Fluids* **2007**, *19*, 117102.
- [61] M. Pilou, S. Tsangaris, P. Neofytou, C. Housiadas, Y. Drossinos, *Aerosol Sci. Technol.* **2011**, *45*, 1376.
- [62] J. B. Mathieu, S. Martel, *Biomed. Microdevices* **2007**, *9*, 801.
- [63] A. Khosravi, M. Malekan, M. E. H. Assad, *Renewable Energy* **2019**, *134*, 54.
- [64] K. E. Peyer, L. Zhang, B. J. Nelson, *Nanoscale* **2013**, *5*, 1259.
- [65] X. Zhang, L. Zheng, M. Luo, C. Shu, E. Wang, *Powder Technol.* **2020**, *366*, 63.
- [66] C. A. Basciano, C. Kleinstreuer, A. S. Kennedy, W. A. Dezarn, E. Childress, *Ann. Biomed. Eng.* **2010**, *38*, 1862.
- [67] D. Mukherjee, N. D. Jani, K. Selvaganesan, C. L. Weng, S. C. Shadden, *J. Biomech. Eng.* **2016**, *138(8)*.
- [68] R. Bhaskaran, L. Collins, *Introduction to CFD Basics*, Cornell University, New York **2002**.
- [69] A. Sayma, *Computational Fluid Dynamics*, Sayma & Ventus Publishing, München **2009**.
- [70] S. M. Peker, Ş. Ş. Helvacı, *Solid-Liquid Two Phase Flow*, Elsevier Philadelphia **2008**, pp. 245–289.
- [71] P. C. Sousa, J. Carneiro, R. Vaz, A. Cerejo, F. T. Pinho, M. A. Alves, M. S. N. Oliveira, *Biorheology* **2013**, *50*, 269.
- [72] T. Alexy, E. Pais, R. B. Wenby, W. Hogenauer, K. Toth, H. J. Meiselman, K. R. Kensey, *Clin. Lab.* **2005**, *51*, 523.
- [73] S. Kim, Y. I. Cho, A. H. Jeon, B. Hogenauer, K. R. Kensey, *J. Non-Newtonian Fluid Mech.* **2000**, *94*, 47.
- [74] S. Chien, S. Usami, H. M. Taylor, J. L. Lundberg, M. I. Gregersen, *J. Appl. Physiol.* **1966**, *21*, 81.
- [75] J. W. Haverkort, S. Kenjereš, C. R. Kleijn, *Ann. Biomed. Eng.* **2009**, *37*, 2436.
- [76] K. Belharet, D. Folio, A. Ferreira, *IEEE Int. Conf. Intell. Rob. Syst.* **2012**, *1*, 2559.
- [77] G. J. G. Upton, J. D. Jobson, *Applied Multivariate Data Analysis, Volume 1: Regression and Experimental Design*, Vol. 78, Springer New York, NY **1994**.
- [78] S. Martel, J.-B. Mathieu, O. Felfoul, A. Chanu, E. Aboussouan, S. Tamaz, P. Poupponeau, L. Yahia, G. Beaudoin, G. Soulez, M. Mankiewicz, *Appl. Phys. Lett.* **2007**, *90*, 114105.
- [79] V. Lalande, F. P. Gosselin, M. Vonthron, B. Conan, C. Tremblay, G. Soulez, S. Martel, *Med. Phys.* **2015**, *42*, 969.